Journal of The Electrochemical Society, 2023 **170** 090521

Improving the Long-term Cycle Performance of $xLi_2MnO_3 \cdot (1\text{-}x)LiMeO_2/Li_4Ti_5O_{12}$ Cells via Prelithiation and Electrolyte Engineering

Yicheng Zhang,[1] Glenn Teeter,[1] Young Jin Kim,[2] Kyusung Park,[1] Anthony Burrell,[1] and Yeyoung Ha[1,a,z]

[1]*Materials, Chemical, and Computational Science Directorate, National Renewable Energy Laboratory, 15013 Denver West Parkway, Golden, Colorado 80401, United States of America*
[2]*Battery Materials North America, BASF Corporation, 23800 Mercantile Road, Beachwood, Ohio 44122, United States of America*

Toward the development of high energy density and long lifetime batteries for behind-the-meter storage (BTMS) applications, Li- and Mn-rich layered oxide cathode ($xLi_2MnO_3 \cdot (1\text{-}x)LiMeO_2$, Me = Ni, Mn, and etc., LMR-NM) and $Li_4Ti_5O_{12}$ (LTO) anode system was examined. To mitigate the major degradation mechanisms at each electrode (i.e., loss of Li inventory (LLI) at the anode and transition metal dissolution and oxygen release at the cathode), two approaches were taken—prelithiating the LTO electrode and varying the electrolyte solvent compositions. The effect of prelithiation and electrolyte engineering on the long-term cycle performance of LMR-NM/LTO cells were systematically evaluated via electrochemical analyses and post-mortem characterizations. By using a prelithiated LTO anode and supplying additional Li to the system, the capacity retention of LMR-NM/LTO system was improved. The degree of enhancement was dependent on the types of electrolytes used, as their decomposition products determined the level of LLI. With increased capacity retention, however, the cathode was utilized to a greater extent, resulting in more severe loss of the cathode active material. Thus, all degradation mechanisms should be considered comprehensively when designing high performance LMR-NM/LTO cells to account for their complex interplay.
 [DOI: 10.1149/1945-7111/acf5a7]

Manuscript submitted June 14, 2023; revised manuscript received August 6, 2023. Published September 14, 2023.

Supplementary material for this article is available online

Behind-the-meter storage (BTMS) operates via energy storage systems (ESS) installed at the consumer end which allow the on-site generated energy to be stored and supplied upon demand without going through the electric meter.[1] BTMS is often integrated with solar photovoltaics (PV) and electrical vehicle (EV) fast charging facilities in buildings to provide an optimized energy solution for the electrification of society. By shifting the time of use of electricity, BTMS can improve flexibility and stability of the power system and reduce the electricity cost. Successful BTMS systems require batteries with ultra-long cycle life, good safety, low cost, and relatively high energy density. The high energy density and good cycling stability of lithium (Li)-ion batteries (LiBs)[2–5] along with a significant reduction in their cost achieved in the last decade make them attractive technologies for BTMS.

The long lifetime and enhanced safety of BTMS batteries can be achieved by using lithium titanate ($Li_4Ti_5O_{12}$, LTO) as the anode material. Its "zero-strain" property, which refers to negligible volume changes upon Li insertion and extraction, provides extraordinary long-term cycling stability.[6–8] In addition, LTO exhibits lithiation and delithiation plateaus around 1.55 V vs Li/Li^+.[6,9,10] This high operating potential eliminates possible Li plating and dendrite growth, enhancing the safety and cycle life of batteries.[11,12] On the cathode side, materials operating at a relatively high potential are desired to compesate for the high potential of the LTO anode and provide sufficient energy density. In addition, critical-material-free cathodes are necessary to meet the cost requirements for BTMS. Previously, we evaluated lithium manganese oxide ($LiMn_2O_4$, LMO), a 4 V critical-material-free spinel cathode, paired with LTO anode.[13–15] While the LMO/LTO cells showed excellent cycle stability, limited capacities (~100 mAh g^{-1}) were obtained from the LMO cathode. Li− and manganese (Mn)-rich layered oxide materials ($xLi_2MnO_3 \cdot (1\text{–}x)LiMeO_2$, Me = Ni, Mn, and etc., LMR-NM) are promising candidates to further increase the energy density of full cells as they provide high specific capacities (>250 mAh g^{-1}) and high operating potentials (>4.5 V vs Li/Li^+).[16–18] In our previous work on evaluating the LMR-NM/LTO chemistry for BTMS applications,[19] LMR-NM/LTO cells delivered capacities above 190 mAh $g_{LMR\text{-}NM}^{-1}$ after 500 cycles at C/2 rate which corresponds to ~75% capacity retention. While this is indeed an impressive result, the cycle life can be further improved by mitigating degradation pathways.

The main degradation mechanism at the LTO anode is loss of Li inventory (LLI), which results from the decomposition of electrolyte.[14,20,21] Despite its high operating potential, LTO is reactive toward electrolyte reduction and the decomposition products form a solid electrolyte interphase (SEI) at the anode surface.[10,14,22,23] LLI can be alleviated by tuning the electrolyte properties to form an SEI that can effectively passivate the LTO surface and prevent excess electrolyte decomposition. Another method for improving the capacity retention is supplying additional Li to the system (i.e., prelithiation). There are various prelithiation methods developed for LiBs, especially for materials that experience severe LLI, such as Si- and Sn-based anodes.[24–28] Although prelithiation of LTO is much less explored as the LTO anode already provides a good cycle performance, it can be a promising method to futher improve the long-term capacity retention of LTO-based systems.[14]

At the cathode, transition metal dissolution and oxygen release are the major degradation mechanisms.[19,29–31] Recently, it was reported that ethylene carbonate (EC)-free, ethyl methyl carbonate (EMC)-based electrolytes show better high-voltage (>4.4 V vs Li/Li^+) performance than the conventional EC-based electrolytes for $LiNi_{(1-x-y)}Mn_xCo_yO_2$ (NMC)/graphite full cells.[32–34] Klein et al. demonstrated that the better performance of the EMC-only electrolyte is due to greater amounts of salt decomposition products ($Li_xPO_yF_z$), which can scavenge transition metals in the electrolyte and suppress their deposition at the anode.[32] In addition, Dose et al. showed that oxygen release from the cathode and subsequent degradations are suppressed in the EMC-only electrolyte for Ni-rich layered oxide

[a]Present address: Exponent, Inc., 149 Commonwealth Drive, Menlo Park, California 94025, United States.
[z]E-mail: yha@exponent.com

cathodes.[35] These findings suggest that EMC-only electrolytes could also benefit the performance of LMR-NM cathodes.

In this work, we aim to improve the long-term cycle performance of LMR-NM/LTO cells by engineering the electrolyte and prelithiating the anode. Electrolytes containing lithium hexafluorophosphate ($LiPF_6$) in EC/EMC mixture and EMC-only solvents are examined. The effect of salt concentration on the cell performance, such as Li^+ ion transport properties and the rate capability of the cell,[13] is not considered in this work as the goal is to understand the interplay between the solvent systems and the electrodes, focusing on their ability to passivate the LTO surface and stabilize the cathode performance. In addition, we evaluate the full cell peformance using electrochemically prelithiated LTO anodes, factoring in their interplay with the two electrolytes. Combining detailed electrochemical analyses and post-mortem characterizations, we show that the capacity retention of LMR-NM/LTO cells can be enhanced via prelithiation of the anode. However, the cell performance is highly dependent on the electrolyte and resulting SEI composition. Since lithiated LTO is more reactive than its pristine state,[36,37] failure to create a stable SEI results in accelerated electrolyte decomposition at the prelithiated anode, leading to limited increase in the capacity retention. Moreover, while the overall capacity retention is improved with additional Li inventory, it leads to greater utilization of the cathode, resulting in more severe loss of active material (LAM), which negatively impacts the cell performance. Thus, all degradation pathways should be carefully considered when designing cells as the interconnected mechanisms could show opposite responses.

Experimental

Electrode preparation and cell assembly.—LMR-NM cathodes were prepared by mixing 92.5 wt% active material powder (BASF Corporation), 4 wt% carbon black (Timcal Super C65), and 3.5 wt% polyvinylidene fluoride binder (PVDF, Solvay 5130) in N-Methyl-2-pyrrolidone (NMP, 99.5%, Sigma Aldrich) and coating the slurry on a 20 μm thick aluminum (Al) foil inside an argon (Ar)-filled glovebox. Electrodes were dried at 120 °C under vacuum for 12 h in a vacuum oven attached to the glovebox. Then, the dried electrodes were calendered to have a total thickness of 47–49 μm with an average coating loading of 7.1 mg cm^{-2}. The LTO electrodes were provided by the Cell Analysis, Modeling and Prototyping (CAMP) Facility at Argonne National Laboratory. 87 wt% LTO (SamSung Fine Chemicals Company, Ltd.), 5 wt% C45 conductive carbon (Timcal) and 8 wt% PVDF (Kureha 9300) was coated on a 20 μm thick Al foil, with a total thickness of 122 μm and a coating loading of 14.1 mg cm^{-2}. Half-cell test results of the pristine LMR-NM and LTO electrodes are shown in Supporting Information (Fig. S1). Areal capacities of 1.89 mAh cm^{-2} and 2.05 mAh cm^{-2} are obtained from the LMR-NM and LTO electrodes, respectively, during the second cycle. All electrodes were dried at 120 °C under vacuum prior to use.

CR2032-type coin cells were assembled in an Ar-filled glove box. LMR-NM/LTO full cells consisted of a 14 mm diameter cathode, a 15 mm diameter anode, a 19 mm diameter Celgard 2325 separator, and 70 μl electrolyte. Half-cells consisted of a 14 mm diameter LMR-NM electrode or a 15 mm diameter LTO electrode, a 15.5 mm diameter polished Li metal foil (99.9%, 0.75 mm thick, Alfa Aesar), a 19 mm diameter Celgard 2325 separator, and 70 μl electrolyte. 1.2 M $LiPF_6$ in EC/EMC (3:7, w/w) (Gen2, Tomiyama Pure Chemical Industries, Ltd.) and 1.0 M $LiPF_6$ (>99.99%, Sigma Aldrich) in EMC (Tomiyama Pure Chemical Industries, Ltd.) were used as electrolytes.

To assemble prelithiated full cells, LTO electrodes were first electrochemically prelithiated in half-cells by applying 0.74 mA current and 0.3 mAh capacity limit. Then, the half-cell was disassembled in an Ar-filled glove box and the retrieved LTO electrode was paired with a pristine LMR-NM cathode to make a full cell. Reassemble experiments of cycled full cells were performed by disassembling the full cells, retrieving cycled anodes and cathodes, and assembling half-cells with the retrieved electrodes. Prior to the cycled cell reassembly, all retrived electrodes were soaked in 2 ml dimethyl carbonate (DMC) for 1 min and residual DMC was evaporated under the glove box environment.

Electrochemical testing.—Coin cells were tested using a MACCOR Series 4000 Automated Test System. All cells were placed in a MACCOR MTC-020 temperature chamber set to 45 °C.

LMR-NM/LTO full cells were cycled by initially performing two formation cycles, during which the cells were charged with a constant current (CC) at C/15 (1C = 294 mA $g_{LRM\text{-}NM}{}^{-1}$) to an upper cutoff voltage (UCV) of 3.2 V followed by a constant voltage (CV) hold at 3.2 V with a current limit of C/50 (CCCV step). The cells were then CC discharged at C/15 to a lower cutoff voltage (LCV) of 0.5 V. Following the two formation cycles, the cells were CCCV charged to 3.0 V at C/2 rate with C/10 limit. During discharge, 30 s rest followed by 30 s 2C discharge pulse was applied to measure the voltage drop, which was used to calculate the area specific impedance (ASI) at the corresponding state of charge (SOC). After the 2C pulse, cells were rested for 30 s and then discharged at C/2 rate until 1/10 of the discharge capacity of the previous cycle was reached, followed by 5 min rest. The 30 s rest, 30 s 2C discharge, 30 s rest, C/2 rate discharge, and 5 min rest sequence was repeated 10 times or until the cell voltage reached the 0.5 V LCV, which completed the third cycle. The cells were then cycled 49 times at C/2 rate between 0.5 and 3.0 V with CCCV charge (C/10 limit) and CC discharge. The ASI measurement cycle and 49 aging cycles were repeated 10 times, resulting in total 500 cycles. Finally, two additional cycles at C/15 rate with voltage window of 0.5–3.0 V with CCCV charge (C/50 limit) and CC discharge were performed to complete the test.

Reassembled half-cells were cycled five times at C/15 rate (1C = 294 mA $g_{LMR\text{-}NM}{}^{-1}$, same as the full cell) where the LTO and LMO half-cells started with a lithiation and delithiation half-cycle, respectively. LTO/Li cells were cycled between 1.0 and 2.5 V, and LMR-NM/Li cells were cycled between 2.0 and 4.5 V with a voltage hold at 4.5 V until the current became smaller than C/50.

Post-mortem analyses.—Once the electrochemical test protocol was completed, the full cells were disassembled in an Ar-filled glove box to retrieve the cycled electrodes. The retrieved electrodes were soaked in 2 ml DMC for 1 min and dried under dynamic vacuum for 1 h prior to post-mortem analyses. Scanning electron microscopy (SEM) images were collected using a Hitachi S-4800 SEM operated at an acceleration voltage of 6 kV and a current of 5 μA. X-ray photoelectron spectroscopy (XPS) measurements were performed by a Physical Electronics Phi VersaProbe III with monochromatic Al Kα X-ray excitation ($h\upsilon$ = 1.487 keV). XPS data processing and curve fitting were carried out using a custom program based on Igor Pro software previously described.[38]

Results and Discussion

Electrochemical performance of full cells.—The first cycle voltage profiles and dQ/dV curves of LMR-NM/LTO full cells with and without prelithiated LTO anodes containing Gen2 and EMC-only electrolytes are shown in Fig. 1. Charge and discharge capacity values and Coulombic efficiencies are provided in Table S1. Comparing the Gen2 cells, slightly smaller capacity is obtained during the first charge from the prelithiated cell (321.1 and 303.8 mAh g^{-1} from the cells without and with prelithiation, respectively). Taking a closer look at the voltage profiles, the two traces overlap until 3.0 V and then start to diverge, where the prelithiated cell exhibits a steeper slope and results in a smaller capacity obtained in this voltage range. The difference is also observed in the dQ/dV plot where the peak above 3.0 V is smaller in the prelithiated cell. This voltage range corresponds to the activation of Li_2MnO_3 in the LMR-NM cathode to MnO_2

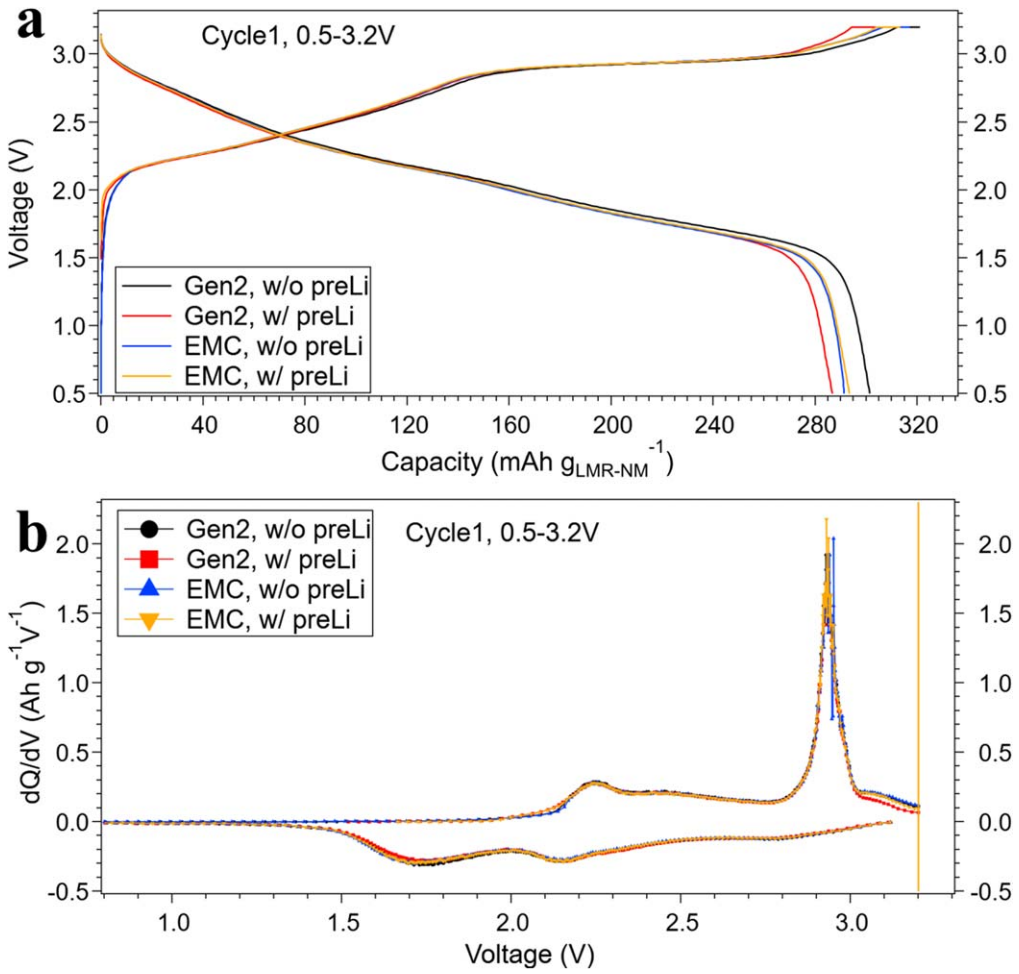

Figure 1. (a) First cycle voltage profiles and (b) dQ/dV curves of LMR-NM/LTO cells with and without prelithiation containing Gen2 and EMC-only electrolytes. Cells were cycled between 0.5 and 3.2 V with CCCV charge (C/50 limit) and CC discharge at C/15 rate (1C = 294 mA g_{LMR-NM}^{-1}). All tests were performed at 45 °C.

($Li_2MnO_3 \rightarrow Li_2O + MnO_2$), which takes place at ~4.5 V vs Li/Li^+ (equivalent to ~3.0 V vs LTO) during the first charge process.[16,39,40] Due to this limited cathode activation, the prelithiated cell shows a smaller capacity during the discharge (301.3 and 286.7 mAh g^{-1} from the cells without and with prelithiation, respectively). The LTO anode was prelithiated by applying 0.3 mAh capacity limit (0.17 mAh cm^{-2}), which decreases its available capacity from 2.08 mAh cm^{-2} to 1.91 mAh cm^{-2}. The areal capacities obtained from Gen2 cells without and with prelithiation during first charge are 2.07 and 1.88 mAh cm^{-2}, respectively, which correlate with the available LTO capacity.

The EMC cells, on the other hand, show similar charge and discharge capacities with and without prelithiation, and the values lie between the capacities of Gen2 prelithiated and non-prelithiated cells. Gen2 and EMC-only cells were fabricated exactly the same except the type of electrolyte, and the electrodes in each cell have similar loadings (Table S1). Thus, the differences observed between Gen2 and EMC-only systems can be attributed to the electrolyte properties. For example, the ionic conductivity of EMC-only electrolyte (6.26 mS cm^{-1}) is lower than that of the Gen2 electrolyte (12.36 mS cm^{-1}) at 45 °C (Fig. S2) which could be causing the smaller capacity of the EMC cell for the non-prelithiated case. However, an opposite trend is observed for the prelithiated case (EMC cell exhibits higher capacity than the Gen2 cell) indicating there are other factors affecting the cell performance. For example, different compositions of the surface layers created from the two electrolytes could affect the activation of cathode and the performance of anode.

Figure S3 shows zoomed-in dQ/dV profiles in the 0.1–2.0 V voltage range during the first charge. A small oxidation peak appears at ~1.5 V from the non-prelithiated EMC cell, which can be attributed to decomposition reactions of the EMC-only electrolyte. This peak is absent from the non-prelithiated Gen2 cell, indicating the presence of EC in the electrolyte alters decomposition pathways. Similar behavior was observed previously from NMC/graphite full cells containing 1 M $LiPF_6$ in EMC electrolyte, which exhibited a strong peak between 3.1 and 3.2 V due to the decomposition of EMC at the anode during the first charge.[34,41] The peak disappeared when cyclic carbonates, such as EC, were added to the electrolyte, as they formed a passivating layer on the graphite surface preventing the EMC reduction. EC has a similar effect on the LTO anode as well,[14] which will be further discussed in the later section along with post-mortem characterization results. Another noticeable feature in this plot is the difference between prelithiated and non-prelithiated cells, where the prelithiated cells show higher open circuit voltage (OCV) values compared to the non-prelithiated cells. This ~1.4 V voltage difference can be attributed to the different anode potentials—prelithiated LTO will be at its plateau (~1.55 V vs Li/Li^+) while the OCV of pristine LTO electrodes are ~2.6 V vs Li/Li^+.

Figure 2 shows the long-term cycle performance of Gen2 and EMC cells with and without prelithiation. For both Gen2 and EMC electrolytes, prelithiated cells exhibit better capacity retention than the non-prelithiated cells after 500 cycles, demonstrating that the additional Li inventory can successfully mitigate the capacity loss due to LLI. Comparing the first and last C/2 rate cycles (cycle 4 and 502), prelithiated and non-prelithiated Gen2 cells show 81% and

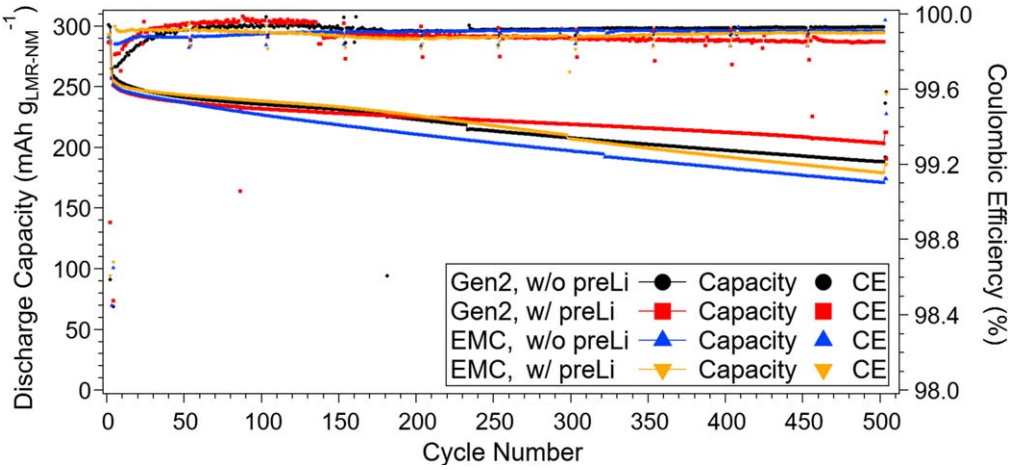

Figure 2. Long-term cycle performance of LMR-NM/LTO cells with and without prelithiation containing Gen2 and EMC-only electrolytes. Discharge capacities (mAh g^{-1}) and Coulombic efficiencies (CE, %) are plotted as a function of cycle number. Cells were cycled at C/15 rate for two cycles followed by 500 cycles at C/2 rate, and ended with final two cycles at C/15 rate (1C = 294 mA g_{LRM-NM}^{-1}). Voltage range of 0.5–3.2 V was used for the first two cycles and 0.5–3.0 V was used for the rest. All tests were performed at 45 °C.

73% capacity retention, respectively, and prelithiated and non-prelithiated EMC cells show 70% and 68% capacity retention, respectively. Thus, while both electrolytes exhibit enhanced capacity retention with prelithiation, the extent is greater when using Gen2 electrolyte. Gen2 electrolyte shows a superior performance to the EMC-only electrolyte when there is no prelithiation, and as a result the prelithiated EMC cell shows a smaller capacity than the non-prelithiated Gen2 cell at the end of the 500 cycles.

Another common behavior observed from the prelithiated cells is a larger increase in the discharge capacity when the C-rate is changed from C/2 to C/15 at the end of cycling compared to the non-prelithiated cell of the same electrolyte. This observation indicates there is a greater impedance growth in the prelithiated cells. Indeed, higher ASI values are observed from the prelithiated cells (Fig. S4). The difference between ASI values of prelithiated and non-prelithiated cells is negligible initially, but it becomes noticeable upon cycling as the ASI of prelithiated cells exhibit a faster rise. The higher impedance of prelithiated cells can also be correlated with the evolution in their Coulombic efficiencies. During the first ~150 cycles, prelithiated cells exhibit higher Coulombic efficiencies compared to the non-prelithiated cell of the same electrolyte, as the Li consumed in parasitic reactions during charge can be restored using the excess Li in the anode. However, upon cycling, the non-prelithiated cells start to show higher Coulombic efficiencies since the extra Li inventory in prelithiated cells will be exhausted at some point. In addition, other degradation mechanisms such as LAM can become more dominant and affect the Coulombic efficiency in these later cycles. Degradation mechanisms and their impact on the full cell performance will be discussed in more detail in the following section with half-cell reassembly experiment results.

Voltage profiles and dQ/dV curves of the 50th and the 500th cycles are shown in Fig. 3. For the Gen2 electrolyte, the prelithiated and non-prelithiated cells exhibit overlapping dQ/dV profiles at the 50th cycle. A slightly smaller capacity of the prelithiated cell observed from the voltage profile can be attributed to the limited cathode activation during the first cycle (Fig. 1). After 500 cycles, the dQ/dV peaks during charge exhibit varying degrees of voltage shift and intensity decrease. Distinct differences between the prelithiated and non-prelithiated Gen2 cells are observed during discharge, where the non-prelithiated cell exhibits a sharp drop in the voltage profile below 1.3 V while the prelithiated cell exhibits a gradual slope and provides additional capacity in this lower voltage region (Figs. 3a and 3b). The prelithiated cell exhibits a greater polarization compared to the non-prelithiated cell, which could be caused by the increase in the impedance and/or irreversible cathode structure changes, such as layered-spinel phase transformation.[30,39]

For the EMC-only electrolyte, the prelithiated and non-prelithiated cells exhibit differences at the 50th cycle, where a smaller dQ/dV peak at ~1.6 V during charge and a steeper tail in the voltage profile at the end of discharge are observed from the non-prelithiated cell. After 500 cycles, the ~1.6 V dQ/dV peak during charge becomes negligible from both cells and other dQ/dV peaks also exhibit decrease in their intensities. While the prelithiated EMC cell exhibits higher capacity and larger polarization in the lower voltage region during the discharge similar to the behavior observed from the Gen2 cells, the magnitude of the difference between the prelithiated and non-prelithiated cells is much less. The limited capacity increase with prelithiation from the EMC cells indicates a severe LLI occurring upon cycling. Moreover, both the non-prelithiated and prelithiated EMC cells exhibit smaller polarization compared to the corresponding Gen2 cells (Figs. 3b and 3d) suggesting a relatively mild irreversible structural degradation from the EMC-only electrolyte considering the similar level of the impedance values of the cycled cells containing the two different electrolytes (Fig. S4).

Half-cell reassembly and degradation mode analysis.—To analyze the degradation mechanisms, half-cells were assembled using LTO and LMR-NM electrodes retrieved from the cycled full cells. Figure 4 shows reassembled LTO half-cell voltage profiles. Additionally, a Gen2 full cell was disassembled after the initial formation cycles and the reassembled LTO half-cell result is shown in Fig. S5a. The first lithiation capacities of reassembled half-cells after formation show a noticeable difference between the prelithiated and non-prelithiated cells. The prelithiated cell capacity is 13.6 mAh g_{LTO}^{-1} (=0.295 mAh) smaller than the non-prelithiated cell capacity, and the difference is very close to the amount of Li pre-stored in the LTO electrode (0.3 mAh). Thus, the prelithiated Li is well preserved during the half-cell disassembly and full cell assembly process, and it is hardly lost during the formation cycles. Looking at the reassembled Gen2 cells after 504 cycles (Fig. 4a), the electrodes cycled with and without prelithiation show similar first lithiation capacities (164.7 and 164.9 mAh g_{LTO}^{-1} with and without prelithiation, respectively), indicating all pre-stored Li was consumed during cycling. The capacities are slightly smaller than the first lithiation capacity of the half-cell reassembled after formation (166.9 mAh g_{LTO}^{-1}), and the difference can be attributed to the loss of active material. The cycled prelithiated cell electrode shows a more gradual increase at the end of the voltage profiles suggesting a slightly higher impedance compared to the cycled non-prelithiated cell electrode, but overall the two reassembled LTO Gen2 half-cells exhibit similar behavior.

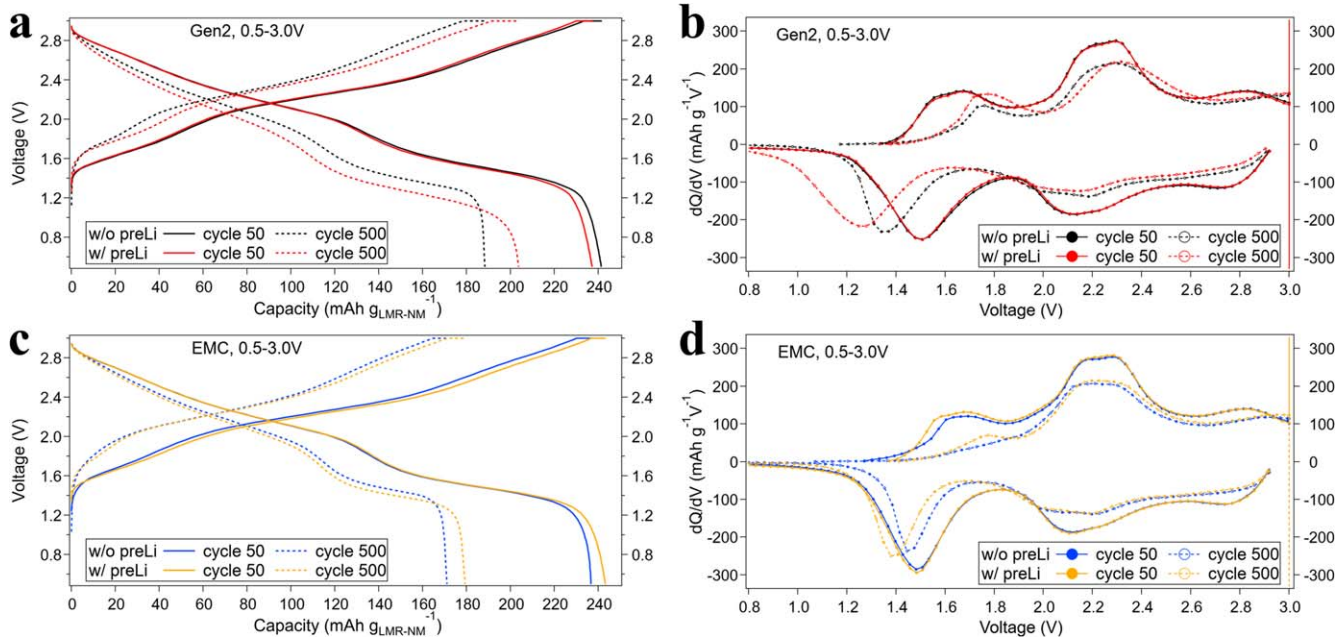

Figure 3. (a), (c) Voltage profiles and (b), (d) dQ/dV curves of LMR-NM/LTO cells with and without prelithiation containing (a), (b) Gen2 and (c), (d) EMC-only electrolytes at the 50th and the 500th cycles. Corresponding cycle results are shown in Fig. 2.

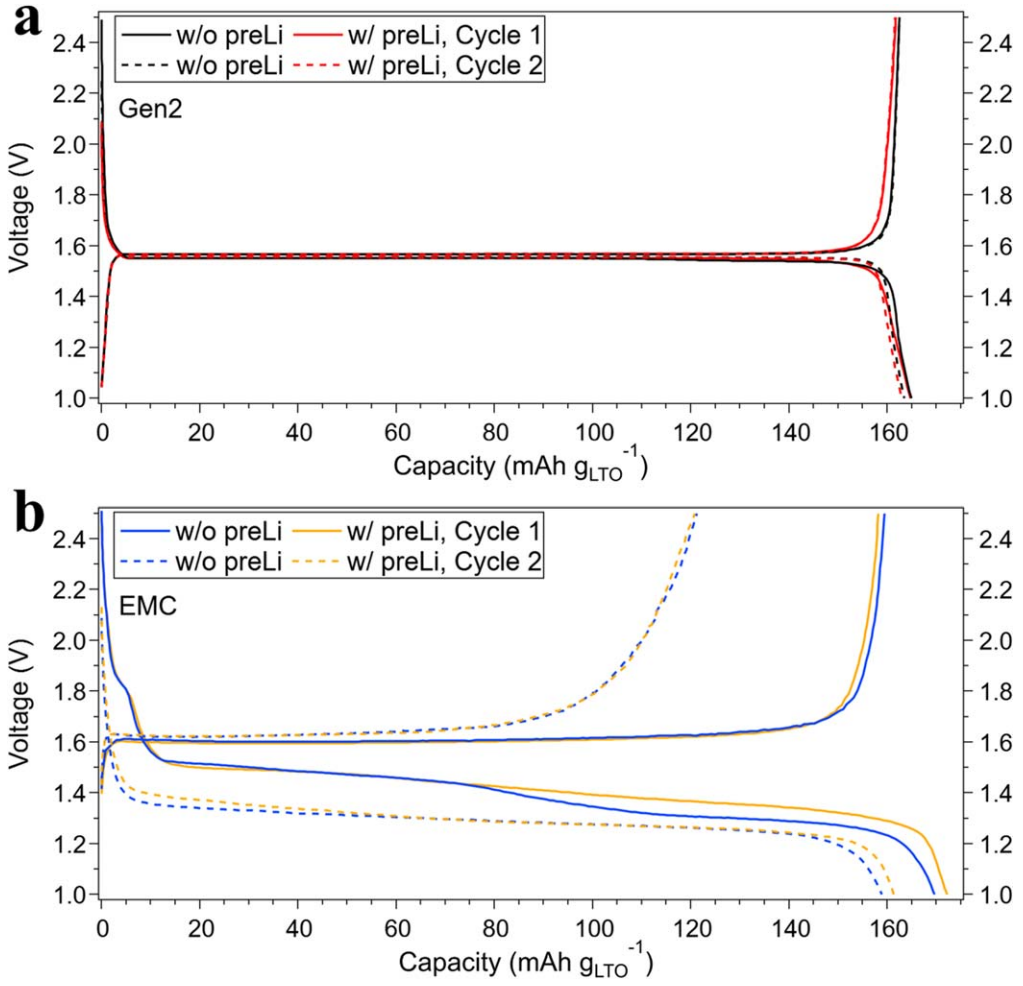

Figure 4. Voltage profiles of LTO/Li half-cells containing electrodes cycled in (a) Gen2 and (b) EMC-only electrolytes with and without prelithiation. Half-cells are fabricated with the same electrolyte that each electrode was cycled in. Cells were lithiated and then delithiated at C/15 rate (1C = same as the full cell) between 1.0 and 2.5 V, repeated two cycles.

Half-cells containing LTO electrodes cycled in EMC full cells (Fig. 4b) show distinctly different voltage profile shapes compared to the Gen2 cells. First, a small plateau appears at ~1.8 V during the first lithiation, which can be attributed to the lithiation of TiO_2.[42–44] This peak is absent when a pristine LTO electrode is lithiated (Fig. S6), indicating the formation of TiO_2 occurs during the long-term cycling. The EMC-cycled LTO half-cells also show large lithiation over potentials and the cell capacities rapidly decrease. This fast failure could be attributed to the aged LTO electrodes and/or the incompatibility between Li metal and the EMC electrolyte. Although the voltage profiles of pristine LTO electrode showed a more stable performance during the first two cycles (Fig. S6), its overpotential also increased especially during the lithiation half-cycles. Moreover, when Li/Li symmetric cells containing Gen2 and EMC electrolytes were cycled (Fig. S7), the EMC-containing cell exhibited a significantly larger polarization than the Gen2-containing cell. Thus, the rapid failure of reassembled LTO half-cells containing EMC-only electrolyte can be attributed to both Li metal effect as well as the degradation products on the cycled electrode.

Figure 5 shows reassembled half-cells of cycled LMR-NM electrodes. Reassembled cathode half-cells after the formation cycles in Gen2 full cells are shown in Fig. S5b. Although the prelithiated full cell showed a slightly smaller capacity during the initial cycles compared to the non-prelithiated full cell due to limited cathode utilization (Figs. S5c and 1), discharge capacities obtained from the reassembled half-cells after the first charge up to 4.5 V show similar values, indicating the prelithiation of LTO does not lead to degradation of the cathode active material during the formation. Electrodes after 504 cycles, on the other hand, show clear difference between prelithiated and non-prelithiated cells. The reassembled LMR-NM half-cells containing cathodes retrieved from the Gen2 full cells (Figs. 5a and 5b) exhibit a larger first charge capacity (206.5 and 183.8 mAh g^{-1} with and without prelithiation, respectively) and a lower OCV (2.98 and 3.10 V with and without prelithiation, respectively) from the prelithiated cell (Table S2). These differences can be attributed to the extra Li inventory in the LTO anode mitigating LLI in the full cell. For example, Li loss during charge will result in less Li returning to the cathode during discharge, leaving the cathode at a partially charged state (i.e., higher OCV). However, when the anode is prelithiated, the cathode can be fully discharged as additional Li is available from the anode.

Once the reassembled cathode goes through one full charge and discharge cycle, the second charge capacity is no longer affected by the LLI from the full cell. Thus, the second charge capacity reflects the full capacity obtained from the remaining active material, and the difference between the 2nd and the 1st charge capacities can be correlated with the magnitude of LLI in the full cell. Both reassembled cells show increasing second cycle capacities, even the cathode cycled with the prelithiated LTO electrode, as all extra Li inventory was consumed during cycling (Fig. 4a). However, the non-prelithiated cell shows a greater difference between the two charge capacities (25.6 and 56.9 mAh g^{-1} with and without prelithiation, respectively). Interestingly, when the pre-stored capacity (0.3 mAh or 31.6 mAh g^{-1}) is added to the 25.6 mAh g^{-1} capacity difference observed from the prelithiated cell cathode, the value (57.2 mAh g^{-1}) becomes close to the charge capacity difference obtained from the non-prelithiated cell cathode (56.9 mAh g^{-1}). This result indicates that the magnitude of LLI is similar regardless of the prelithiation state of the anode for the LMR-NM/LTO full cell containing Gen2 electrolyte.

The reassembled LMR-NM half-cells containing EMC cathodes (Figs. 5c and 5d) also show a larger first charge capacity and a lower OCV from the prelithiated cell cathode, but the difference is much smaller compared to the that observed from the Gen2 cells. The capacity and OCV values are listed in Table S2. Similar behavior of the prelithiated and non-prelithiated cell cathodes indicate that the extra Li inventory was rapidly exhausted via parasitic reactions, failing to benefit the long-term capacity retention. As LTO is more reactive toward (electro)chemical decomposition of the electrolyte when lithiated,[36,37] LLI will be accelerated in the prelithiated full cell unless the LTO surface is successfully passivated. Thus, these results indicate that the SEI formed in the EMC electrolyte is unstable and leads to continuous electrolyte decomposition, while that formed in the Gen2 electrolyte can stabilize the LTO surface and protect the Li inventory. The severe LLI of the EMC electrolyte is also manifested in the full cell cycle result (Fig. 2), where the capacity enhancement observed with prelithiation was much less from the EMC cells compared to the Gen2 cells. We note that unlike

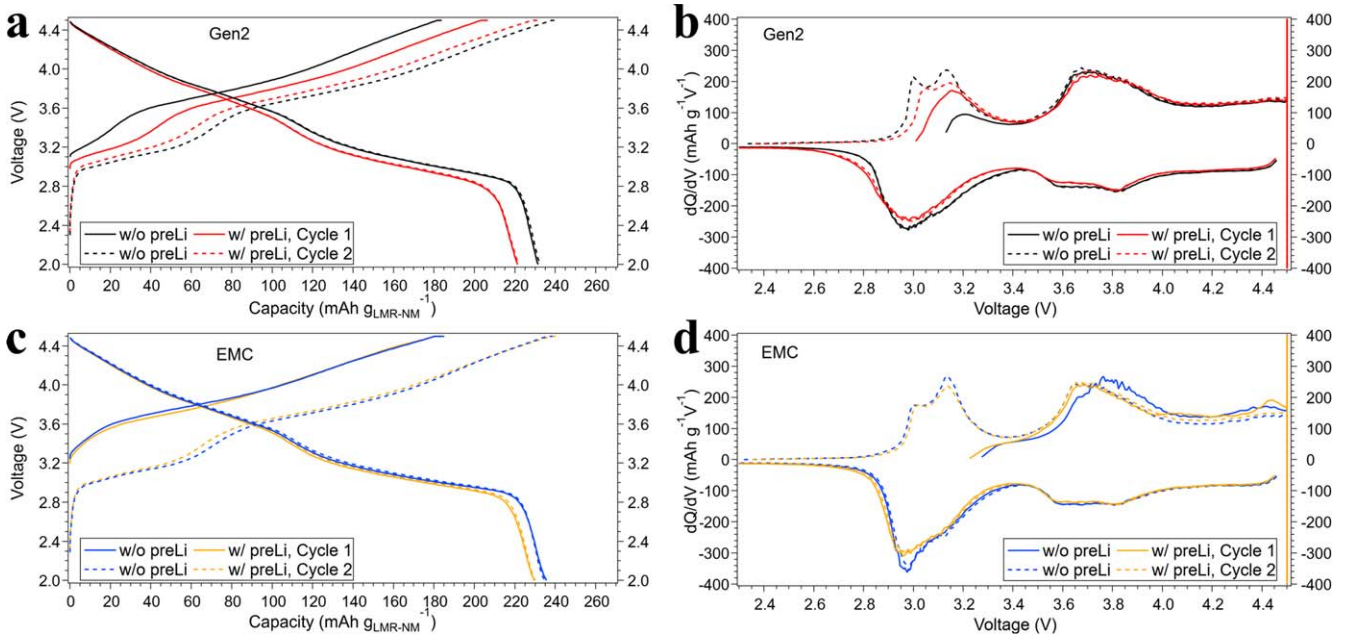

Figure 5. (a), (c) Voltage profiles and (b), (d) dQ/dV curves of LMR-NM/Li half-cells containing electrodes cycled in (a), (b) Gen2 and (c), (d) EMC-only electrolytes with and without prelithiation. Half-cells are fabricated with the same electrolyte that each electrode was cylced in. Cells were delithiated and then lithiated at C/15 rate (1C = same as the full cell) between 2.0 and 4.5 V with a voltage hold at 4.5 V until the current became smaller than C/50, repeated two cycles.

the reassembled LTO half-cells, the cathode half-cells containing EMC electrolyte do not exhibit rapid increase in the polarization and cell failure. The difference could be due to different degradation products on the anode vs cathode surfaces. Also, while Li stripping happens during the first half-cycle in the LTO/Li cells, Li deposition takes place in the LMR-NM/Li cells, which could result in different Li morphologies and affect the overall half-cell performance.

Another degradation mode that can be evaluated from the reassembled cathode half-cells is LAM by analyzing the discharge capacities (Figs. 5a and 5c). Both Gen2 and EMC electrolytes exhibit smaller discharge capacities (i.e., greater LAM) from the prelithiated cell cathodes, and the difference between the prelithiated and non-prelithiated cells is greater in the Gen2 electrolyte. This trend is opposite from the full cell performance (Fig. 2), where the Gen2 with prelithiation exhibited the highest capacity and the EMC without prelithiation exhibited the lowest capacity among the four cells. Thus, the greater LAM can be correlated with more active material utilization during cycling, which is reflected as higher average discharge capacity over the 504 cycles (Table S2). Comparing the discharge capacities of the Gen2 cycled cathode half-cells (Fig. 5a) with the reassembled cells after formation (Fig. S5b), the difference is 41.7 and 33.9 mAh $g_{LMR\text{-}NM}{}^{-1}$ for the prelithiated and non-prelithiated cell cathodes, respectively. These values are greater than the difference calculated from the reassembled LTO half-cells (Figs. S5a and 4a), which are 2.2 and 2.0 mAh $g_{LTO}{}^{-1}$ for the prelithiated and non-prelithiated Gen2 cells, respectively. Thus, the cathodes exhibit more severe LAM compared to the anodes. LAM is also manifested in the dQ/dV profiles (Figs. 5b and 5d), which exhibit intensity changes in multiple peaks. If LLI were the only degradation mode, all features would remain the same except the lower voltage dQ/dV peak decaying due to the OCV shifting higher.[14,20] Although assigning detailed mechanisms for each peak changes is beyond the scope of this work, the degree of LAM in different electrolytes with and without prelithiation is clearly demonstrated in the dQ/dV plots. Finally, the prelithiated cells exhibit a greater polarization during discharge compared to the non-prelithiated cells containing the same electrolyte, which agrees with the higher impedance rise observed from the prelithiated full cell upon cycling (Fig. S4).

The cathode LAM is also observed from XRD patterns of the cycled cathodes shown in Fig. S8. The diffraction peaks are indexed based on a rhombohedral phase with a layered $R\bar{3}m$ space group α-NaFeO2-type structure.[45,46] All cycled cathodes exhibit a shift in the (018) peak to a lower 2θ value (i.e., a larger d-spacing) compared to the pristine electrode, indicating a layered-spinel structure transformation.[47–49] In addition, a new peak appears between the (018) and (110) peaks in the cycled electrodes, which can be indexed as a (440) peak of a cubic spinel phase, futher supporting the layered-spinel transformation.[46,47] Interestingly, the ratio between the cubic (440) peak and rhombohedral (110) peak is larger from the electrodes cylced in the Gen2 electrolyte compared to those cycled in the EMC-only electrolyte, suggesting greater cathode degration of the Gen2 cells.

Post-mortem characterizations.—To understand the origin of varying performance observed from prelithiated vs non-prelithiated and Gen2 vs EMC cells, cycled full cells were disassembled and the retrieved electrodes were characterized via microscopic and spectroscopic techniques.

SEM images of LTO and LMR-NM electrodes presented in Fig. 6 show the morphology of electrodes. First, looking at the LTO images, the pristine electrode (Fig. 6a) consists of multifaceted LTO active material exhibiting smooth surface and sharp edges, and smalller conductive carbon particles distributed throughout the electrode coating. The active material in the Gen2 without prelithiation electrode (Fig. 6b) also exibits smooth surface, but the particle edges are less defined, indicating the electrode is likely covered with a relatively uniform surface layer. The EMC without prelithiation electrode (Fig. 6d, on the other hand, has scattered islands-like features on the LTO particles which exhibit sharp edges. Electrodes from prelithiated cells show similar surface texture as the non-prelithiated cell of the same electrolyte (i.e., smooth layer in Gen2 (Fig. 6c) and island-like morphology in EMC (Fig. 6e)), with a higher coverage of the islands on the EMC without prelithiation electrode surface.

LMR-NM electrodes also exhibit distinct morphologies depending on the test conditions. While the SEM image of the prisitne electrode shows a clear view of the cathode active material and conductive carbon mixture (Fig. 6f), cycled electrodes are covered with a relatively thick layer appearing as darker areas (Fig. 6g through 6j). Energy dispersive X-ray spectroscopy (EDS) analysis of the Gen2 without prelithiation electrode (Fig. S9) exhibits higher intensities of phosphorous signal from the darker regions. For example, while the oxygen signal traces the active material particles in the corresponding SEM image, the phosphorous signal is more homogeneously distributed and shows highest intensities where the active material particle is covered with a darker area in the SEM image. Although an EDS map of the pristine electrode is not provided, the XPS analysis presented in the next section did not reveal any phosphorous signals from the pristine electrode. Thus, the dark surface layer observed from the cycled electrode likely represents cathode electrolyte interphase (CEI) resulting from the decomposition of electrolyte. The EMC without prelithiation electrode (Fig. 6i) shows much fewer dark areas in the SEM image compared to the Gen2 cycled electrodes, which exhibit similar coverage of the darker area with and without prelithiation (Figs. 6h and 6g, respectively). The EMC with prelithiation electrode (Fig. 6j), on the other hand, exhibits a higher coverage of the darker area compared to the without prelithiation electrode. Thus, less decomposition products are formed on the cathode surface from the EMC electrolyte compared to Gen2, but when the anode is prelithiated the coverage at the cathode increases for the EMC electrolyte.

SEM images revealed different morphologies of electrolyte decomposition products formed on the electrode surface from the two electrolytes and with and without prelithiation of the LTO anode. Chemical compositions of the surface layers were further analyzed with XPS to understand the nature of these decomposition products and demonstrate how they correlate with the electrochemical performance of full cells. The extremely surface sensitive nature of XPS measurements (probe depth 5–10 nm with Al Kα X-rays ($h\upsilon$ = 1.487 keV))[14,40,50] can provide information on the surface layer with minimal bulk signal contributions, and any signals obtained from the active material can be used to estimate the thickness and coverage of the surface layers.

Figure 7 shows XPS spectra of LTO (C 1s, Ti 2p, and P 2p core levels) and LMR-NM electrodes (C 1s, O 1s, and P 2p core levels). Additional core level spectra are presented in Figs. S10 and S11. Strong LTO active material signals (Ti^{4+} $2p_{1/2}$ peak at 465.1 eV and $2p_{3/2}$ peak at 459.5 eV)[51,52] are detected from the pristine LTO electrode, along with the PVDF binder and conductive carbon signals (Fig. 7a). When the electrodes are cycled in Gen2 electrolyte (Figs. 7b and 7c), the Ti^{4+} peaks as well as other pristine electrode signals, such as Ti-O (O 1s, 531.1 eV),[42,53,54] carbon black (C 1s, 284.4 eV), and CF_2 from the binder (F 1s, 688.3 eV)[50,53,55] (Fig. S10) noticeably decrease. Simultaneously, electrolyte decomposition product signals such as C-O containing species and fluorophosphates appear in the C 1s and P 2p core levels, respectively,[14,50,53–57] indicating that the formation of SEI layer is responsible for the reduction of the pristine electrode signals from the cycled Gen2 electrodes.

Electrodes cycled in the EMC electrolyte (Figs. 7d and 7e) show similar electrolyte decomposition species as those observed from the Gen2 electrodes, but their Ti 2p core level spectra exhibit distinct features. While the LTO active material signal was hardly detected from the cycled Gen2 electrodes (both with and without prelithiation), the non-prelithiated EMC electrode shows strong Ti^{4+} peaks. This behavior can be correlated with the morphology of SEI layers observed from the SEM images (Fig. 6), where the Gen2 electrolyte

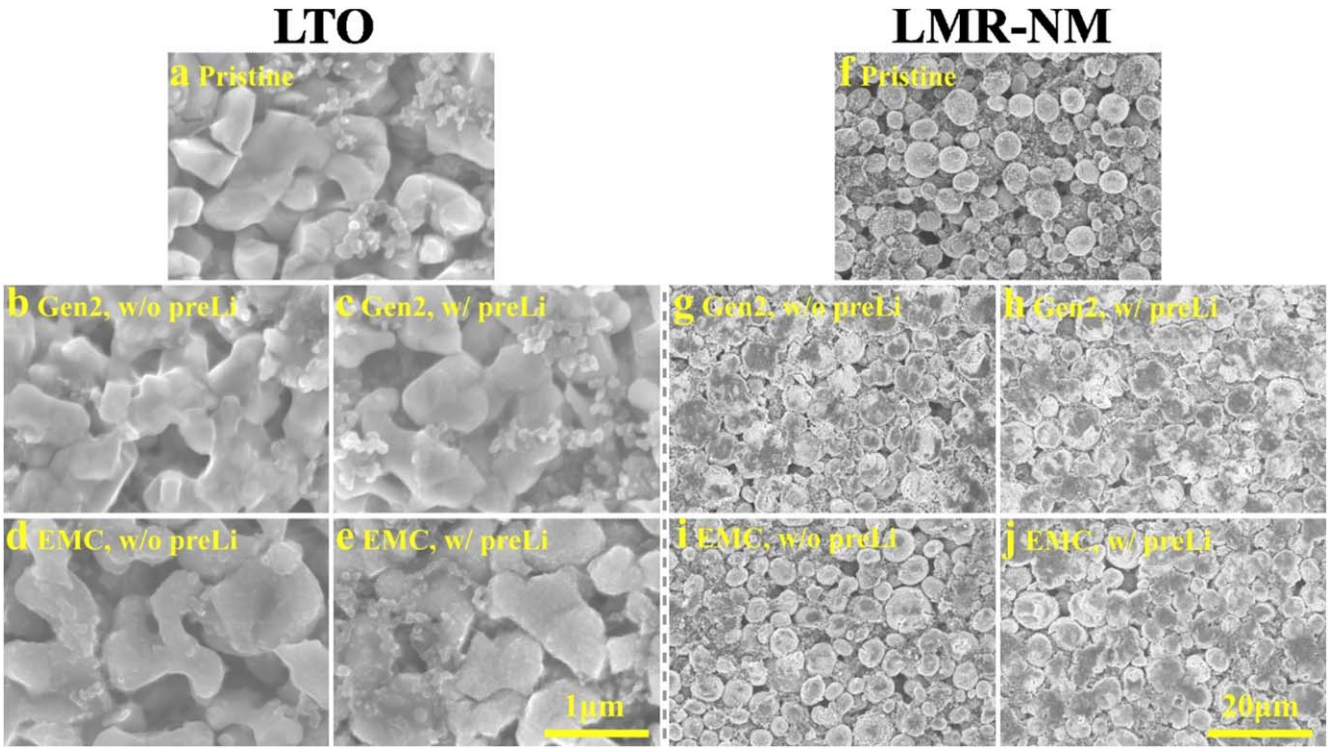

Figure 6. SEM images of LTO (left) and LMR-NM (right) electrodes. (a), (f) Pristine and (b)–(e), (g)–(j) cycled electrodes retrieved from (b), (g) Gen2 without prelithiation, (c), (h) Gen2 with prelithiation, (d), (i) EMC without prelithiation, and (e), (j) EMC with prelithiation full cells after 504 cycles. Images (a)–(e) and (f)–(j) have the same scales as shown in images e and j, respectively.

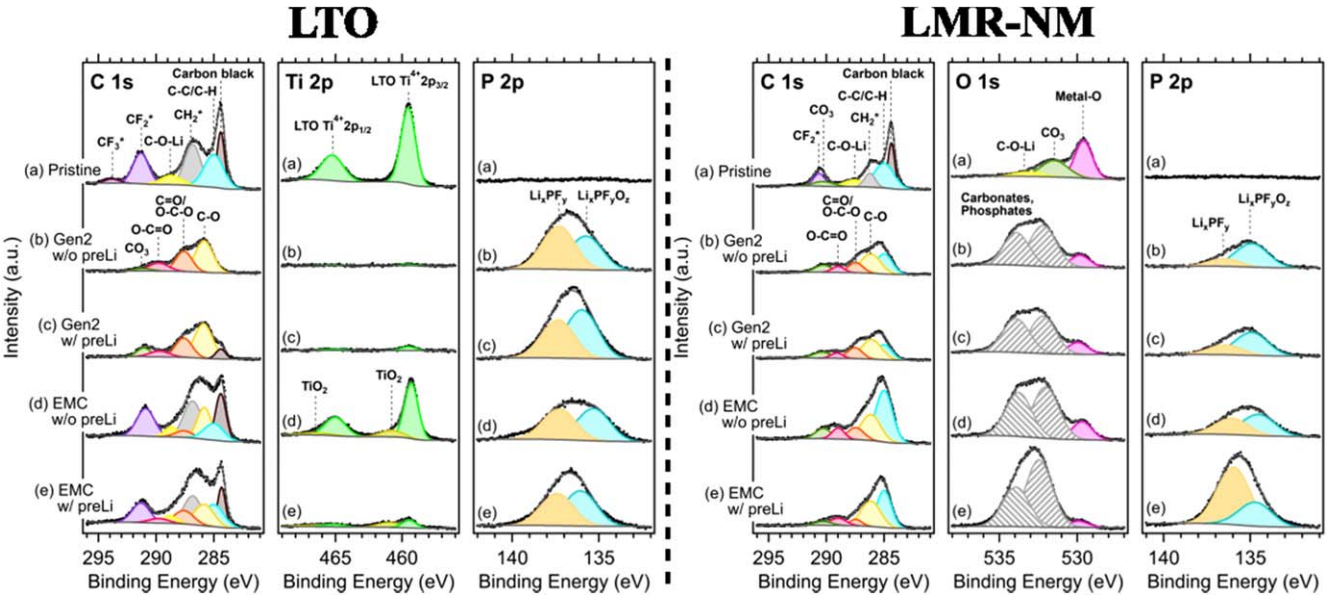

Figure 7. XPS spectra of LTO (left) and LMR-NM (right) electrodes. (a) Pristine and (b)–(e) cycled electrodes retrieved from (b) Gen2 without prelithiation, (c) Gen2 with prelithiation, (d) EMC without prelithiation, and (e) EMC with prelithiation full cells after 504 cycles. C 1s, Ti 2p, and P 2p core levels are presented for the LTO electrodes, and C 1s, O 1s, and P 2p core levels are presented for the LMR-NM electrodes.

formed a uniform layer and the EMC electrolyte created island-like features. Bare LTO surface exposed between the islands are detected as strong Ti^{4+} signals from the EMC without prelithiation electrode. On the other hand, the prelithiated EMC electrode exhibits weak Ti^{4+} peaks, which also agrees with the SEM images where the coverage of island-like features increased on the EMC with prelithiation LTO electrode. Continuous electrolyte decomposition at the exposed LTO active material sites was manifested as LLI in the full cells (Figs. 4 and 5). The different morphologies of the SEI layers formed in the Gen2 and EMC electrolytes can be attributed to different organic species created from these electrolytes. Comparing the C 1s core level spectra, stronger C=O/O–C–O (287.7 eV) and O–C=O (289.8 eV) peaks[14,50,57] are detected from the Gen2 electrodes. These peaks represent the presence of poly(ethylene oxide)-type species resulting from the polymerization of EC,[58–60] which has been shown to benefit the performance of LTO

anodes.[14,61] The severe decomposition of EMC electrolyte due to the lack of protective SEI layer on the LTO surface also leads to the formation of TiO_2 species,[36,62] which are detected as additional peaks in the Ti 2p core level spectra (Figs. 7d and 7e) at 466.5 eV and 460.9 eV.[63,64] The presence of TiO_2 in the LTO electrodes cycled in EMC electrolyte was also observed from the reassembled half-cells (Fig. 4b) as a plateau at ∼1.8 V during the first lithiation.

On the cathode side, a strong metal-O (M-O) peak from the active material is detected from the pristine electrode (O 1s, 529.7 eV)[4,12] and this peak appears in the O 1s core level spectra of all cycled electrodes, indicating that relatively thin and/or porous CEI layers are formed on the cathode surface. Intensities of Ni 2p and Mn 2p signal (Fig. S11) show the same trend as the M-O peak intensities from different electrodes. The EMC without prelithiation electrode exhibits strongest M-O peak among the cycled electrodes, which agrees with the SEM image of this electrode showing the least coverage of darker regions which represented the CEI (Fig. 6). Although the intensities of active material signals vary among the cycled electrodes, the differences are much less compared to the intensity variations of Ti^{4+} peaks observed from the anodes. Also, the organic species of CEI layers show similar compositions in the C 1s core level spectra. Similar salt decomposition products are observed from all cycled electrodes as well, although the prelithiated EMC electrode shows strongest $LiPF_6$ salt decomposition signals such as Li_xPF_y (P 2p, 136.7 eV and F 1s, 688.7 eV) and LiF (F 1s, 685.0 eV) (Fig. S11)[14,50,54] due to its thicker CEI layer.

Conclusions

In this work, we evaluated the effect of prelithiating the LTO anode on the long-term cycle performance of LMR-NM/LTO cells containing Gen2 and EMC-only electrolytes. Combining electrochemical analyses and post-mortem characterizations, we identified the major degradation mechanisms in prelithiated vs non-prelithiated systems, factoring in the electrolyte properties. By using prelithiated LTO anodes, capacity retention of the LMR-NM/LTO cells containing Gen2 and EMC-only electrolytes were increased by 8% (73 to 81%) and 2% (68 to 70%), respectively, after 500 cycles at C/2 rate performed at 45 °C. The difference between Gen2 and EMC-only electrolytes were attributed to the nature of electrolyte decomposition products formed on the LTO surface, which determined the extent of LLI. Without a good passivating layer on the LTO surface, electrolyte decomposition was accelerated when the anode was prelithiated, and resulted in a limited increase of the capacity retention. Interestingly, the prelithiated cells with good anode passivating layer exhibited a greater cathode active material loss due to their higher utilization. Thus, comprehensive understandings of the degradation mechanisms and how the cell performance reacts to the cell design changes (e.g., prelithiation, choice of electrolyte) should be obtained to develop high performing LMR-NM/LTO cells.

Acknowledgments

This work was authored by the National Renewable Energy Laboratory, operated by Alliance for Sustainable Energy, LLC, for the U.S. Department of Energy (DOE) under Contract No. DE-AC36–08GO28308. Funding provided by the U.S. Department of Energy's Vehicle Technologies Office (VTO) under the Behind-the-Meter Storage (BTMS) Consortium directed by Samuel Gillard and managed by Anthony Burrell. The LTO electrode used in this manuscript is from Argonne's Cell Analysis, Modeling and Prototyping (CAMP) Facility, which is fully supported by the DOE's VTO. The views expressed in the article do not necessarily represent the views of the DOE or the U.S. Government. The U.S. Government retains and the publisher, by accepting the article for publication, acknowledges that the U.S. Government retains a nonexclusive, paid-up, irrevocable, worldwide license to publish or reproduce the published form of this work, or allow others to do so, for U.S. Government purposes.

ORCID

Yeyoung Ha https://orcid.org/0000-0003-2679-2539

References

1. A. Odukomaiya, A. Abu-Heiba, and B. Bekker, *2018 IEEE PES/IAS PowerAfrica*, 640 (2018).
2. M. S. Whittingham, *Nano Lett.*, **20**, 8435 (2020).
3. J. B. Goodenough and K.-S. Park, *J. Am. Chem. Soc.*, **135**, 1167 (2013).
4. M. Li, J. Lu, Z. Chen, and K. Amine, *Adv. Mater.*, **30**, 1800561 (2018).
5. O. Schmidt, A. Hawkes, A. Gambhir, and I. Staffell, *Nat. Energy*, **2**, 17110 (2017).
6. T. Ohzuku, A. Ueda, and N. Yamamoto, *J. Electrochem. Soc.*, **142**, 1431 (1995).
7. X. Lu et al., *Adv. Mater.*, **24**, 3233 (2012).
8. J.-H. Choi, W.-H. Ryu, K. Park, J.-D. Jo, S.-M. Jo, D.-S. Lim, and I.-D. Kim, *Sci. Rep.*, **4**, 7334 (2014).
9. M.-S. Song, A. Benayad, Y.-M. Choi, and K.-S. Park, *Chem. Commun.*, **48**, 516 (2012).
10. M.-S. Song, R.-H. Kim, S.-W. Baek, K.-S. Lee, K. Park, and A. Benayad, *J. Mater. Chem. A*, **2**, 631 (2014).
11. K.-S. Park, A. Benayad, D.-J. Kang, and S.-G. Doo, *J. Am. Chem. Soc.*, **130**, 14930 (2008).
12. Q. Liu, C. Du, B. Shen, P. Zuo, X. Cheng, Y. Ma, G. Yin, and Y. Gao, *RSC Adv.*, **6**, 88683 (2016).
13. Y. Ha, A. M. Colclasure, S. E. Trask, S. Ahmed, K. L. Gering, A. N. Jansen, A. Burrell, and K. Park, *J. Electrochem. Soc.*, **168**, 110536 (2021).
14. Y. Ha, S. P. Harvey, G. Teeter, A. M. Colclasure, S. E. Trask, A. N. Jansen, A. Burrell, and K. Park, *Energy Storage Mater.*, **38**, 581 (2021).
15. Y. Ha, S. E. Trask, Y. Zhang, A. N. Jansen, and A. Burrell, *J. Electrochem. Soc.*, **170**, 050520 (2023).
16. M. M. Thackeray, S.-H. Kang, C. S. Johnson, J. T. Vaughey, R. Benedek, and S. A. Hackney, *J. Mater. Chem.*, **17**, 3112 (2007).
17. X. Yu et al., *Adv. Energy Mater.*, **4**, 1300950 (2014).
18. J. R. Croy, A. Gutierrez, M. He, B. T. Yonemoto, E. Lee, and M. M. Thackeray, *J. of Power Sources*, **434**, 226706 (2019).
19. Y. Zhang, G. Teeter, Y. J. Kim, A. Burrell, and K. Park, *Journal of Energy Storage*, **64**, 107226 (2023).
20. C. R. Birkl, M. R. Roberts, E. McTurk, P. G. Bruce, and D. A. Howey, *J. Power Sources*, **341**, 373 (2017).
21. F. Holtstiege, A. Wilken, M. Winter, and T. Placke, *Phys. Chem. Chem. Phys.*, **19**, 25905 (2017).
22. N. Gauthier, C. Courrèges, J. Demeaux, C. Tessier, and H. Martinez, *Appl. Surf. Sci.*, **501**, 144266 (2020).
23. Y. Zhang, G. Teeter, N. S. Dutta, S. Frisco, and S.-D. Han, *Chem. Eng. J.*, **460**, 141239 (2023).
24. Y. Shen, J. Zhang, Y. Pu, H. Wang, B. Wang, J. Qian, Y. Cao, F. Zhong, X. Ai, and H. Yang, *ACS Energy Lett.*, **4**, 1717 (2019).
25. H. J. Kim, S. Choi, S. J. Lee, M. W. Seo, J. G. Lee, E. Deniz, Y. J. Lee, E. K. Kim, and J. W. Choi, *Nano Lett.*, **16**, 282 (2016).
26. F. Li, G. Wang, D. Zheng, X. Zhang, C. J. Abegglen, H. Qu, and D. Qu, *ACS Appl. Mater. Interfaces*, **12**, 19423 (2020).
27. R. Zhan, X. Wang, Z. Chen, Z. W. Seh, L. Wang, and Y. Sun, *Adv. Energy Mater.*, **11**, 2101565 (2021).
28. F. Holtstiege, P. Bärmann, R. Nölle, M. Winter, and T. Placke, *Batteries*, **4**, 4 (2018).
29. C. Zhan, T. Wu, J. Lu, and K. Amine, *Energy Environ. Sci.*, **11**, 243 (2018).
30. E. Hu et al., *Nat. Energy*, **3**, 690 (2018).
31. S.-L. Cui, Y.-Y. Wang, S. Liu, G.-R. Li, and X.-P. Gao, *Electrochim. Acta*, **328**, 135109 (2019).
32. S. Klein, S. van Wickeren, S. Röser, P. Bärmann, K. Borzutzki, B. Heidrich, M. Börner, M. Winter, T. Placke, and J. Kasnatscheew, *Adv. Energy Mater.*, **11**, 2003738 (2021).
33. W. Li, A. Dolocan, J. Li, Q. Xie, and A. Manthiram, *Adv. Energy Mater.*, **9**, 1901152 (2019).
34. L. Ma, S. L. Glazier, R. Petibon, J. Xia, J. M. Peters, Q. Liu, J. Allen, R. N. C. Doig, and J. R. Dahn, *J. Electrochem. Soc.*, **164**, A5008 (2017).
35. W. M. Dose, I. Temprano, J. P. Allen, E. Björklund, C. A. O'Keefe, W. Li, B. L. Mehdi, R. S. Weatherup, M. F. L. De Volder, and C. P. Grey, *ACS Appl. Mater. Interfaces*, **14**, 13206 (2022).
36. J. Liu, P. Bian, J. Li, W. Ji, H. Hao, and A. Yu, *J. Power Sources*, **286**, 380 (2015).
37. R. Bernhard, S. Meini, and H. A. Gasteiger, *J. Electrochem. Soc.*, **161**, A497 (2014).
38. K. N. Wood and G. Teeter, *ACS Appl. Energy Mater.*, **1**, 4493 (2018).
39. J. R. Croy, M. Balasubramanian, K. G. Gallagher, and A. K. Burrell, *Acc. Chem. Res.*, **48**, 2813 (2015).
40. G. Assat, D. Foix, C. Delacourt, A. Iadecola, R. Dedryvère, and J.-M. Tarascon, *Nat. Commun.*, **8**, 2219 (2017).
41. J. Xia, R. Petibon, D. Xiong, L. Ma, and J. R. Dahn, *J. Power Sources*, **328**, 124 (2016).
42. J.-Y. Liao, V. Chabot, M. Gu, C. Wang, X. Xiao, and Z. Chen, *Nano Energy*, **9**, 383 (2014).
43. M. Ding, H. Liu, X. Zhao, L. Pang, L. Deng, and M. Li, *RSC Adv.*, **7**, 43894 (2017).
44. J. H. Jeong, B.-H. Park, G.-W. Lee, K. C. Roh, and K.-B. Kim, *Energy Storage Mater.*, **25**, 510 (2020).
45. Z. Lu, D. D. MacNeil, and J. R. Dahn, *Electrochem. Solid-State Lett.*, **4**, A191 (2001).
46. D. Mohanty, S. Kalnaus, R. A. Meisner, K. J. Rhodes, J. Li, E. A. Payzant, D. L. Wood, and C. Daniel, *J. Power Sources*, **229**, 239 (2013).

47. D. Mohanty, J. Li, D. P. Abraham, A. Huq, E. A. Payzant, D. L. I. Wood, and C. Daniel, *Chem. Mater.*, **26**, 6272 (2014).
48. Y. Li, M. Bettge, B. Polzin, Y. Zhu, M. Balasubramanian, and D. P. Abraham, *J. Electrochem. Soc.*, **160**, A3006 (2013).
49. E.-S. Lee, A. Huq, H.-Y. Chang, and A. Manthiram, *Chem. Mater.*, **24**, 600 (2012).
50. N. Schulz, R. Hausbrand, C. Wittich, L. Dimesso, and W. Jaegermann, *J. Electrochem. Soc.*, **165**, A833 (2018).
51. R. T. Haasch and D. P. Abraham, *Surf. Sci. Spectra*, **26**, 014012 (2019).
52. M. C. Biesinger, B. P. Payne, B. R. Hart, A. P. Grosvenor, N. S. McIntryre, L. W. Lau, and R. S. Smart, *J. Phys. Conf. Ser.*, **100**, 012025 (2008).
53. N. Gauthier, C. Courrèges, J. Demeaux, C. Tessier, and H. Martinez, *J. Power Sources*, **448**, 227573 (2020).
54. J.-B. Gieu, C. Courrèges, L. El Ouatani, C. Tessier, and H. Martinez, *J. Power Sources*, **318**, 291 (2016).
55. N. Gauthier, C. Courrèges, L. Goubault, J. Demeaux, C. Tessier, and H. Martinez, *J. Electrochem. Soc.*, **165**, A2925 (2018).
56. D. Ensling, M. Stjerndahl, A. Nytén, T. Gustafsson, and J. O. Thomas, *J. Mater. Chem.*, **19**, 82 (2009).
57. R. Tatara, P. Karayaylali, Y. Yu, Y. Zhang, L. Giordano, F. Maglia, R. Jung, J. P. Schmidt, I. Lund, and Y. Shao-Horn, *J. Electrochem. Soc.*, **166**, A5090 (2019).
58. A. M. Andersson and K. Edström, *J. Electrochem. Soc.*, **148**, A1100 (2001).
59. J. Henschel, C. Peschel, S. Klein, F. Horsthemke, M. Winter, and S. Nowak, *Angew. Chem. Int. Ed.*, **59**, 6128 (2020).
60. S. J. An, J. Li, C. Daniel, D. Mohanty, S. Nagpure, and D. L. Wood, *Carbon*, **105**, 52 (2016).
61. L. Wen, Z. Wu, P. Zhao, J. Liang, H. Luo, G. Liu, and F. Li, *J. Electrochem. Soc.*, **166**, A5033 (2019).
62. Y.-B. He et al., *Sci. Rep.*, **2**, 913 (2012).
63. M.-S. Balogun, Y. Zhu, W. Qiu, Y. Luo, Y. Huang, C. Liang, X. Lu, and Y. Tong, *ACS Appl. Mater. Interfaces*, **7**, 25991 (2015).
64. T. Ji, Y. Liu, H. Zhao, H. Du, J. Sun, and G. Ge, *J. Solid State Chem.*, **183**, 584 (2010).